Composite Structures 368 (2025) 119290

Contents lists available at ScienceDirect

Composite Structures

journal homepage: www.elsevier.com/locate/compstruct

Reconfigurable metamaterial honeycomb sandwich panels based on embedded tube Helmholtz resonators

Hui Wang [a], Yaxiang Sun [a], Xin Lan [a], Hanxing Zhao [a,*], Yong-Hua Yu [c], Weichun Huang [c], Yanju Liu [b,*], Jingsong Leng [a]

[a] Centre for Composite Materials and Structures, Harbin Institute of Technology, Harbin 150080, People's Republic of China
[b] Department of Aerospace Engineering and Mechanics, Harbin Institute of Technology, Harbin 150001, People's Republic of China
[c] National Laboratory of Solid State Microstructures & Collaborative Innovation Center of Advanced Microstructures, Nanjing University, Nanjing 210093, China

ARTICLE INFO

Keywords:
Acoustic metamaterial
Embedded tube Helmholtz resonator
SMP
Tunable acoustic characteristics

ABSTRACT

Acoustic metamaterials depend on the geometry and spatial distribution of their microstructure, which is difficult to change without an external mechanical load after manufacturing, which limits their application in complex mechanical environments. Based on the sound insulation mechanism of traditional Helmholtz resonators, the resonant frequency of embedded tube Helmholtz resonators is theoretically deduced in this paper, and the regulatory relationship between the structural parameters and their acoustic characteristics (transmission loss) is derived. Then, using the shape memory effect of the shape memory polymers (SMPs), reconfigurable embedded tube Helmholtz resonators with various temporary configurations are designed. On this basis, reconfigurable metamaterial honeycomb sandwich panels with reconfigurable microstructures and adjustable macroacoustic performance are further constructed. Through simulations and experiments, the excellent sound insulation performance of reconfigurable metamaterial honeycomb sandwich panels in different configurations is verified. In addition, the sound insulation performance of honeycomb sandwich panels with the same arc length but different wave numbers and different bottom configurations is analysed in detail. This study plays an important role in guiding the application of acoustic metamaterials in complex mechanical environments.

1. Introduction

With the proliferation of high-thrust engines in modern transportation systems, including aircraft, naval vessels, carrier rockets, and other heavy-duty transport platforms operating under extreme velocity and payload conditions, the resultant acoustic radiation during operation have reached critical levels. This escalating noise not only affects the health of the operator and reduces the accuracy and reliability of the equipment but also poses a threat to the equipment stealth [1]. Traditional sound insulation materials have difficulty providing effective protection against low-frequency noise with high energy and large wavelengths. Therefore, researchers have proposed the concept of "acoustic metamaterials" based on the study of phonon crystals, which are used to achieve low-frequency sound absorption/insulation and acoustic target intensity control [2–5]. Acoustic metamaterials are complex artificial materials constructed by means of functional primitives and spatial ordering, which can exhibit remarkable acoustic properties that are not present in conventional sound insulation materials, leading to their extensive application in the field of noise mitigation and protection. Currently, acoustic metamaterials include the membrane type [6], local resonance type [7,8], Helmholtz resonance type [9], space-coiled type [10], etc. Generally, by designing the microscopic configuration of a structure, the macroscopic equivalent mass density or equivalent bulk modulus of the structure is negative within a certain frequency range, thus forming a band gap, effectively attenuating sound waves, and realizing "small size control of a large wavelength." Jang et al. designed an innovative acoustic metamaterial that utilizes the unique acoustic properties of membranes and local resonant structures in sound insulation to improve low-frequency and broadband acoustic performance [11]. Du et al. summarized the design methods of typical acoustic metamaterials from the perspective of structural design, which provides the sound absorption function through equivalent negative parameter and bandgap characteristics [12]. Ma et al. reviewed the development of acoustic metamaterials, pointing out that many new structures are generated by the collective manifestations of constituent resonating units and that these novel structures further

---

* Corresponding authors.
E-mail addresses: zhaohxhit@126.com (H. Zhao), yj_liu@hit.edu.cn (Y. Liu).

https://doi.org/10.1016/j.compstruct.2025.119290
Received 18 December 2024; Received in revised form 7 April 2025; Accepted 15 May 2025

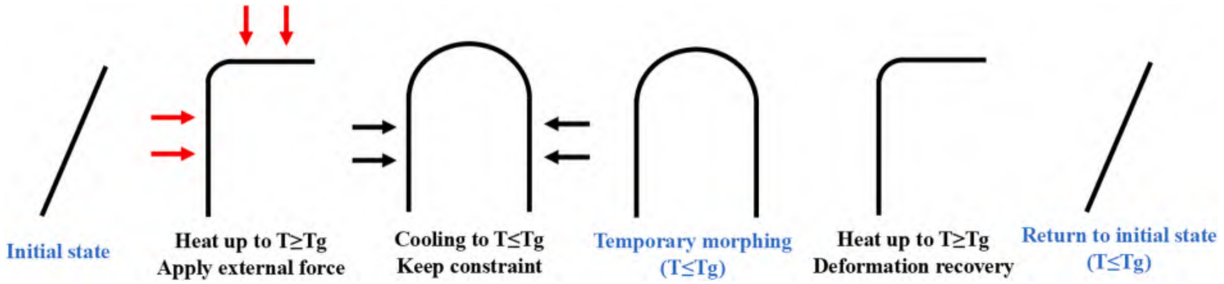

Fig. 1.1. SMP shape memory cycle diagram.

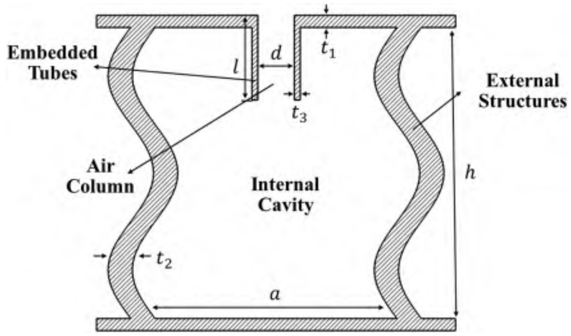

Fig. 2.1. Structural diagram of the embedded tube Helmholtz resonator.

extend wave manipulation functionalities [13]. Liu et al. proposed and studied a curved double wall metamaterial with local resonance to improve its sound insulation performance by designing a narrowband metamaterial that matches the double wall characteristic frequency [14]. Xin et al. constructed a labyrinthine acoustic metamaterial consisting of eight resonance units. Based on the analysis of the valley value and peak value principle of the sound insulation curve, an ultrasparse distribution hypersurface was designed, and high-efficiency sound insulation was achieved at 417 Hz [15]. Langfeldt et al. introduced the Helmholtz resonator into a plate-type acoustic metamaterial. A sound insulation peak was added due to the resonance mechanism of the Helmholtz resonator, thus significantly extending the sound insulation band [16]. An acoustic metamaterial that combines the lightweight properties of a honeycomb sandwich with the Helmholtz resonance mechanism was proposed by Gai et al. By deeply exploring the regulatory relationship between structural parameters and sound insulation performance, the structural parameters of the acoustic metamaterial were optimized, and the low-frequency noise control problem of thin-layer lightweight structures was effectively solved [17].

As a common acoustic metamaterial, Helmholtz resonators can effectively suppress and regulate sound in a specific frequency range [18]. Although the traditional Helmholtz resonator can achieve the sound absorption effect at large wavelengths under small sizes, its sound absorption peak is often sharp, and the sound absorption band is narrow. Longer pipes or larger cavity volumes often improve low-frequency sound absorption, but this not only increases manufacturing costs but also limits its application in limited space [19]. Based on the traditional structure, Sharafkhani et al. proposed a new design. The single-band sound absorber based on the Helmholtz resonator is converted to a multiband sound absorber while maintaining its thickness [20]. To broaden the bandwidth, Wei et al. connected four Helmholtz resonators in parallel and realized perfect multiunit sound absorption by optimizing the structural parameters [21]. Hu et al. designed a Helmholtz-type acoustic metamaterial with a double-sided complex “S” channel. Research has shown that the complexity of the “S” channel improves the low-frequency sound insulation performance of the resonator [22]. Huang et al. reported that an embedded tubular Helmholtz resonator greatly improved the system impedance control ability, significantly reduced the perfect absorber thickness, and verified its subwavelength sound absorption ability through theoretical analysis and experimental verification of the acoustic system [23]. Hu et al. proposed a new acoustic metamaterial that combines a thin film, labyrinth and Helmholtz resonator. Through simulation and experimental analysis, the metamaterial shows excellent broadband sound insulation performance [24].

As a passive design structure, the characteristics of acoustic metamaterials depend on the geometry and spatial distribution of their microstructure, and it is difficult to change their acoustic properties without external mechanical loads after manufacturing [25], which limits the application of acoustic metamaterials in complex mechanical environments. Therefore, the development of reconfigurable acoustic metamaterials with reconfigurable microstructures and adjustable macroscopic acoustic properties is urgently needed to improve their application flexibility and adaptability. The appearance of shape memory polymers (SMPs) provides a new opportunity for the development of reconfigurable acoustic metamaterials. As a multiexcitation response material, SMPs can detect changes in the external environment and actively respond to these alterations, thereby facilitating the shape memory cycle of “initial state-temporary morphing-return to initial state” (Fig. 1.1). With adaptive and self-driven capabilities, SMP is an ideal raw material for reconfigurable acoustic metamaterials [26–36]. In addition, 4D printing technology, as an important extension of 3D printing, its core feature is that additive manufacturing of dynamic structures can be achieved. This type of intelligent structure can achieve active control of shape, performance or function in response to external environmental stimuli, such as temperature, humidity, light or magnetic field [37–39]. Based on this technical advantage, the combination of shape memory polymer (SMP) and fused deposition melding (FDM) 4D printing technology provides a key technical support for the development of acoustic metamaterials with intelligent tunable acoustic properties.

Therefore, the resonance frequency of embedded tube Helmholtz resonators is first theoretically deduced based on the sound insulation mechanism of traditional Helmholtz resonators in this paper, and the regulatory relationship between the structural parameters and their acoustic characteristics (transmission loss) is derived. Then, using the SMP active deformation characteristic, reconfigurable embedded tube Helmholtz resonators whose cavity wall configuration can change with the external environment (temperature) are designed. On this basis, a metamaterial honeycomb sandwich panel composed of several reconfigurable resonators is constructed to make the microstructure reconfigurable and the macroacoustic performance adjustable. Finally, on the basis of the theoretical and simulation results, a reconfigurable metamaterial honeycomb sandwich panel whose acoustic characteristics can be intelligently and actively controlled was prepared via 4D printing technology, and its acoustic performance was verified. In addition, the sound insulation performance of honeycomb sandwich panels with the same arc length but different wave numbers and different bottom configurations is analysed in detail. The reconfigurable metamaterial honeycomb sandwich panels demonstrate significant potential for

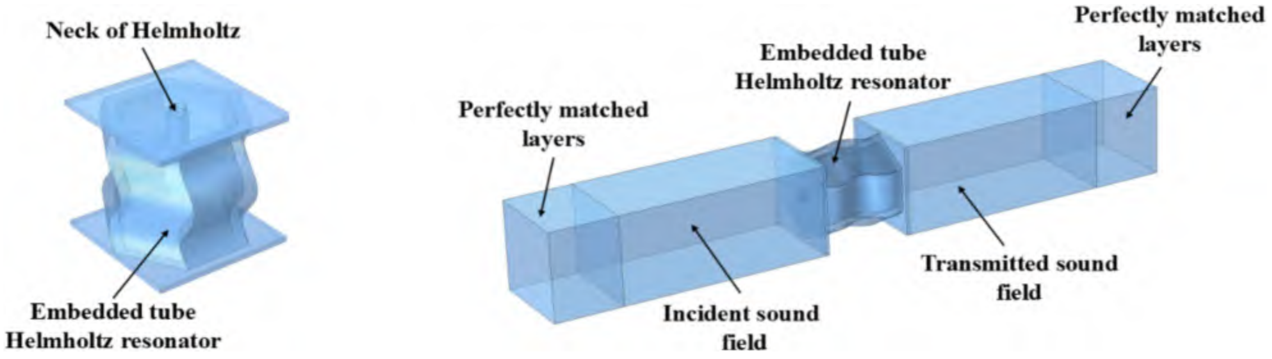

Fig. 3.1. Perspective and finite element model of the embedded tube Helmholtz resonator.

Table 3.1
Structure parameters of the embedded tube Helmholtz resonator.

l(mm)	d(mm)	t_1(mm)	t_2(mm)	t_3(mm)	a(mm)	h(mm)
6	3	1	2	0.5	12	24

intelligent tunable acoustic properties, including tunable acoustic liners for aerospace structures (enabling frequency-selective noise suppression in aircraft engine nacelles), deployable temperature-responsive noise barriers for smart buildings, and dynamically tunable underwater acoustic stealth coatings for marine equipment.

2. Theoretical analysis model of the embedded tube Helmholtz resonator

The embedded tube Helmholtz resonator consists of four parts: a cylindrical embedded tube, an air column in the tube, an internal air cavity and an external structure, as shown in Fig. 2.1. The specific structural parameters include the cylindrical embedded tube length l, cylindrical embedded tube diameter d, cylindrical embedded tube wall thickness t_3, upper and lower plate wall thicknesses of the external structure t_1, body wall thickness of the external structure t_2, regular hexagon side length a and cavity height h.

The traditional Helmholtz resonator is often regarded as an independent acoustic vibration system. The air within the tube will resonate when the incident sound wave frequency matches the natural frequency of the spring–mass system in the cavity, maximizing the sound energy.

Compared with the traditional Helmholtz resonator, the mass of the air column in the embedded tube is M_m, the air in the cavity can be equivalent to a spring, the elastic coefficient is K_m, and the compliance is $C_m = \frac{1}{K_m}$. Let the incident sound pressure at the pipe mouth be $p = P_0 e^{j\omega t}$; then, the mechanical vibration equation of the air column and the cavity can be expressed as:

$$M_m \frac{dv}{dt} + R_m v + \frac{1}{C_m}\int v dt = P_0 e^{j\omega t} \tag{1}$$

When the air column in the tube vibrates, R_m is the frictional resistance between the inner wall of the tube and the air. The time is t, and the velocity of the air column in the tube is v. $S_0 = \frac{\pi d^2}{4}$ is the area of the tube mouth. The force impedance can be expressed as:

$$Z_m = R_m + j\left(\omega M_m - \frac{1}{\omega C_m}\right) \tag{2}$$

$$R_m = \frac{l S_0}{d/2}\sqrt{2\eta\rho_0\omega}, M_m = \rho_0 l S_0, C_m = \frac{V}{\rho_0 c_0^2 S_0^2} \tag{3}$$

The shear viscosity coefficient of air is η, and the value is 1.87×10^{-5}. Since the wavelength of the sound wave is much larger than the length of the embedded tube, the mass of the air column in the tube is modified at the end; that is, l in M_m is replaced by L_k,$L_k = l + \delta$. For a cylinder, δ takes the value $\frac{8}{3\pi} d$[40], which is approximately $0.85d$.

The acoustic vibration system is equivalent to the mechanical vibration system, and the acoustic mass $M_A = \frac{M_m}{S_0^2}$, the sound resistance $R_A = \frac{R_m}{S_0^2}$, and the sound capacity $C_A = C_m S_0^2$ are obtained. For the object studied in this paper, the acoustic resistance R_A and acoustic mass M_A are provided by the air column in the tube, whereas the acoustic capacity C_A is provided by the internal cavity; that is, the acoustic impedance of the tube is as follows:

$$Z_l = R_A + j\omega M_A \tag{4}$$

When $\lambda >> h$, the sound pressure of the entire internal cavity is considered constant, and then, the acoustic impedance of the chamber can be expressed as:

$$Z_V = \frac{p}{v} = \frac{p}{U} = -\frac{j\rho_0 c_0^2}{\omega V} = \frac{1}{j\omega C_A} \tag{5}$$

where the volume of the irregular internal cavity is V, ρ_0 is the air density, and ω is the frequency of the mass system of the spring in the cavity.

Since the folding space is relatively small and it is not a narrow folding space, the deviation calculated in this way is relatively small [40]; then, the expression for the acoustic impedance of the structure can be derived as follows:

$$Z_a = Z_l + Z_v = \frac{2l}{\pi d^3}\sqrt{32\eta\rho_0\omega} + \mathrm{j}\omega\frac{4\rho_0(l+\delta)}{\pi d^2} - \mathrm{j}\frac{\rho_0 c_0^2}{\omega V} \tag{6}$$

When $\mathrm{Im}[Z_a] = 0$, corresponding to the resonance state of the system, the expression of the resonance frequency f_0 can be calculated as:

$$f_0 = \frac{\omega_0}{2\pi} = \frac{dc_0}{2\pi}\sqrt{\frac{\pi}{4VL_k}} = \frac{dc_0}{2\pi}\sqrt{\frac{\pi}{4V(l+0.85d)}} \tag{7}$$

Combined with Eq. (3), the resonance frequency can be expressed as:

$$f_0 = \frac{\omega_0}{2\pi} = \frac{dc_0}{2\pi}\sqrt{\frac{\pi}{4VL_k}} = \frac{c_0}{2\pi}\sqrt{\frac{S_0}{VL_k}} = \frac{1}{2\pi}\sqrt{\frac{1}{M_A C_A}} \tag{8}$$

3. Regulation of transmission loss of an embedded tube Helmholtz resonator by structural parameters

The transmission loss of the embedded tube Helmholtz resonator is calculated via the multiphysics simulation software COMSOL. As Fig. 3.1 shows, the geometric model includes four parts: the PML layer, incident sound field, embedded tube Helmholtz resonator, and transmitted sound field. The structural parameters of the embedded tube Helmholtz resonator are shown in Table 3.1.

In this paper, a finite element simulation of an embedded tube Helmholtz resonator is carried out by coupling a pressure acoustic

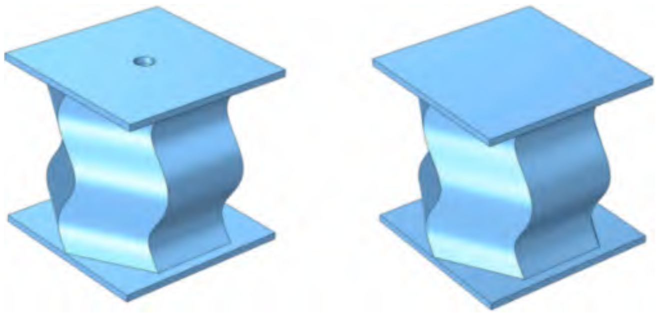

Fig. 3.2. Diagram of the embedded tube Helmholtz resonator and cellular element.

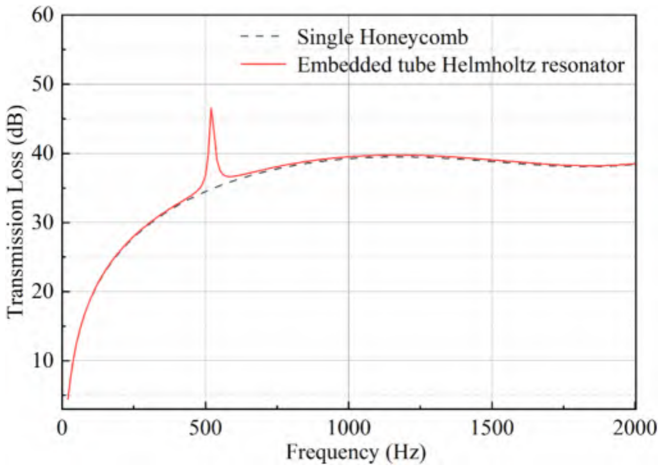

Fig. 3.3. Comparison of transmission losses between the embedded tube Helmholtz resonator and the cellular element.

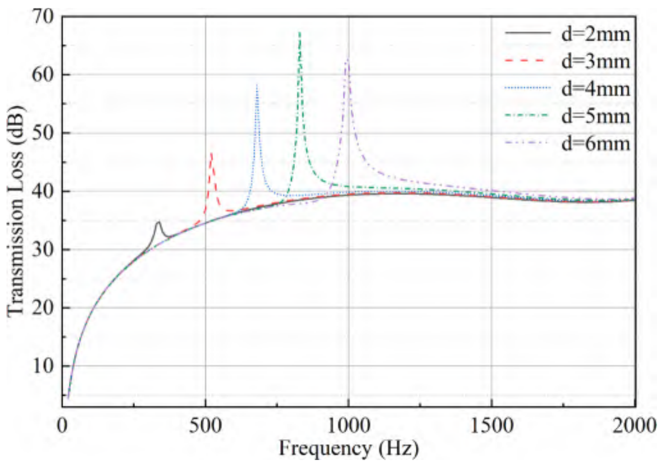

Fig. 3.4. Comparison of transmission losses of embedded tube Helmholtz resonators with different embedded tube diameters.

module, a thermoviscous acoustic module and a solid mechanics module. The external structure material is set as PLA, the background sound pressure field with a sound pressure amplitude of 1 Pa is used as the acoustic excitation for the incident sound field, and the sound wave is vertically incident on the embedded tube Helmholtz resonator. To simulate the infinite sound field, Floquet boundary conditions are set for the front, back, left and right edges of the model. The upper and lower domains are perfectly matched layers, and the sound waves are absorbed as much as possible when incident on the perfectly matched layer. The

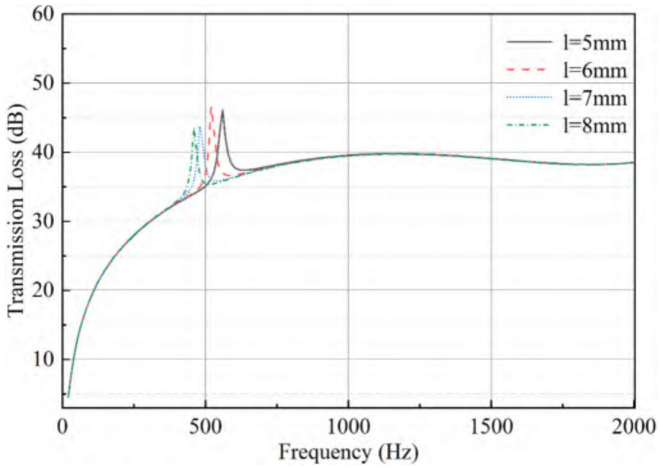

Fig. 3.5. Comparison of the transmission loss of the embedded tube Helmholtz resonators with different embedded tube lengths.

density ρ of PLA is $1248Kg/m^3$, the elastic modulus E is $3.5GPa$, and σ represents the Poisson's ratio with a value of 0.3.

The geometric model is meshed, and the incident sound field, transmitted sound field, internal air cavity and external structure are divided by a free tetrahedral mesh. It is convenient to use a boundary layer mesh to analyze the thermal viscosity acoustic effect of the air column in a tube, and the thermal viscosity loss can be resolved. The perfectly matched layers on both sides are divided by sweeping. To absorb the sound waves incident on the perfectly matched layer as much as possible and prevent the sound waves from repeatedly reflecting, the perfectly matched layer grid should be at least 8 layers. To satisfy the calculation accuracy, at least 5 cell grids are guaranteed in the shortest wavelength.

The boundary between the perfectly matched layer and the incident sound field on the incident side, as well as the boundary between the perfectly matched layer and the transmitted sound field on the transmission side, are integrally processed, and the transmission loss is calculated as follows:

$$\begin{cases} TL = 10\log10(w_{in}/w_{out}) \\ w_{in} = \displaystyle\int \frac{P_i^2}{2\rho c} ds \\ w_{out} = \displaystyle\int \frac{P_t^2}{2\rho c} ds \end{cases} \tag{9}$$

where the incident sound power is w_{in}, P_i represents the amplitude of the sound pressure on the incident sound pressure side, the transmitted sound power is w_{out}, and the amplitude of the sound pressure is P_t on the transmitted sound pressure side. ρ_o and c_0 represent the air density and sound velocity, respectively.

Fig. 3.3 shows the comparative analysis results of transmission loss between the embedded tube Helmholtz resonator and the cellular element [17] (as shown in Fig. 3.2). It is obvious that there is a transmission loss (TL) peak in the relatively narrow frequency band of the embedded tube Helmholtz resonator. This phenomenon occurs primarily because when the frequency of the incident sound wave aligns with the natural frequency of the spring mass system in the cavity, it will cause air resonance in the tube, thereby achieving maximum dissipation of the sound energy, which leads to a substantial increase in transmission loss and the formation of a peak.

The resonance frequency of the embedded tubular Helmholtz resonator reflects the frequency band where peak sound insulation occurs, which is closely associated with the diameter and length of the cylindrical embedded tube. As shown in Fig. 3.4, the resonance frequency of the resonator is directly proportional to the diameter d of the cylindrical

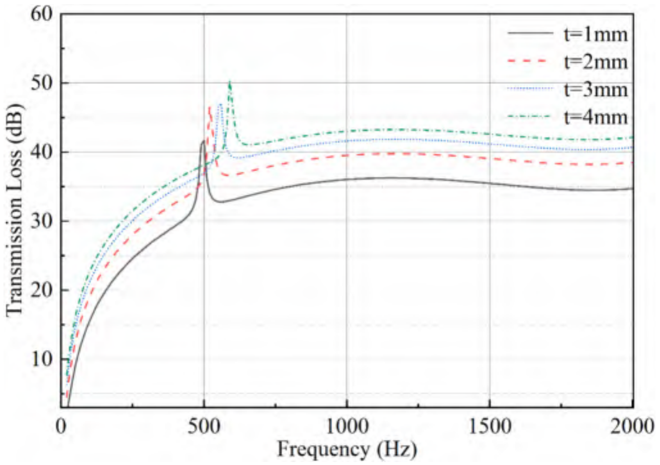

Fig. 3.6. Comparison of the transmission loss of embedded tube Helmholtz resonators with different external structure wall thicknesses.

embedded tub. The primary reason for this phenomenon is that, despite the increase in the cross-sectional area of the sound wave due to the enlarged diameter of the embedded tube, the propagation path of the sound wave is also shortened; that is, the effective length is reduced, and the acoustic mass of the neck of the embedded tube Helmholtz resonator is reduced, thus increasing the resonance frequency. This conclusion is consistent with the variation rule described in Eq. (7), that is, the resonance frequency is proportional to the neck's cross-sectional area (i.e., the diameter of the embedded tube).

According to the comparative analysis of the transmission loss of the embedded Helmholtz resonators with different tube lengths shown in Fig. 3.5, as the length *l* of the cylindrical tube increases, the resonance frequency tends to decrease. This phenomenon occurs mainly because as the length of the embedded tube *l* increases, the acoustic mass increases, and the resonance frequency decreases. This process adheres to the working principle of a resonator and is analogous to the dynamic characteristic of a "mass–spring" system. This conclusion aligns with the change rule described in Formula (7), which further verifies the correctness of the theoretical model.

In addition, the resonant frequency is related to the thickness of the external structure of the resonator. As shown in Fig. 3.6, this section explores the effect of the difference in the thickness of the external structure of the resonator on the transmission loss. The data analysis revealed that the larger the external structure wall thickness is, the greater the resonance frequency, and the better the overall acoustic performance. In contrast, the thinner the external structure is, the lower the first resonance frequency leading to poor overall acoustic performance. This relationship is also evident in the equivalent model; that is, as the thickness of the external structure thickens, the volume of the inner cavity decreases, resulting in a higher resonance frequency f_0, which is conducive to regulating the resonance frequency. However, owing to the sinusoidal configuration of the resonator cavity wall, if the wall is too thick, it will lead to collision inside the cavity, resulting in structural deformation. Therefore, the external structure wall thickness must be reasonably designed to optimize its sound insulation

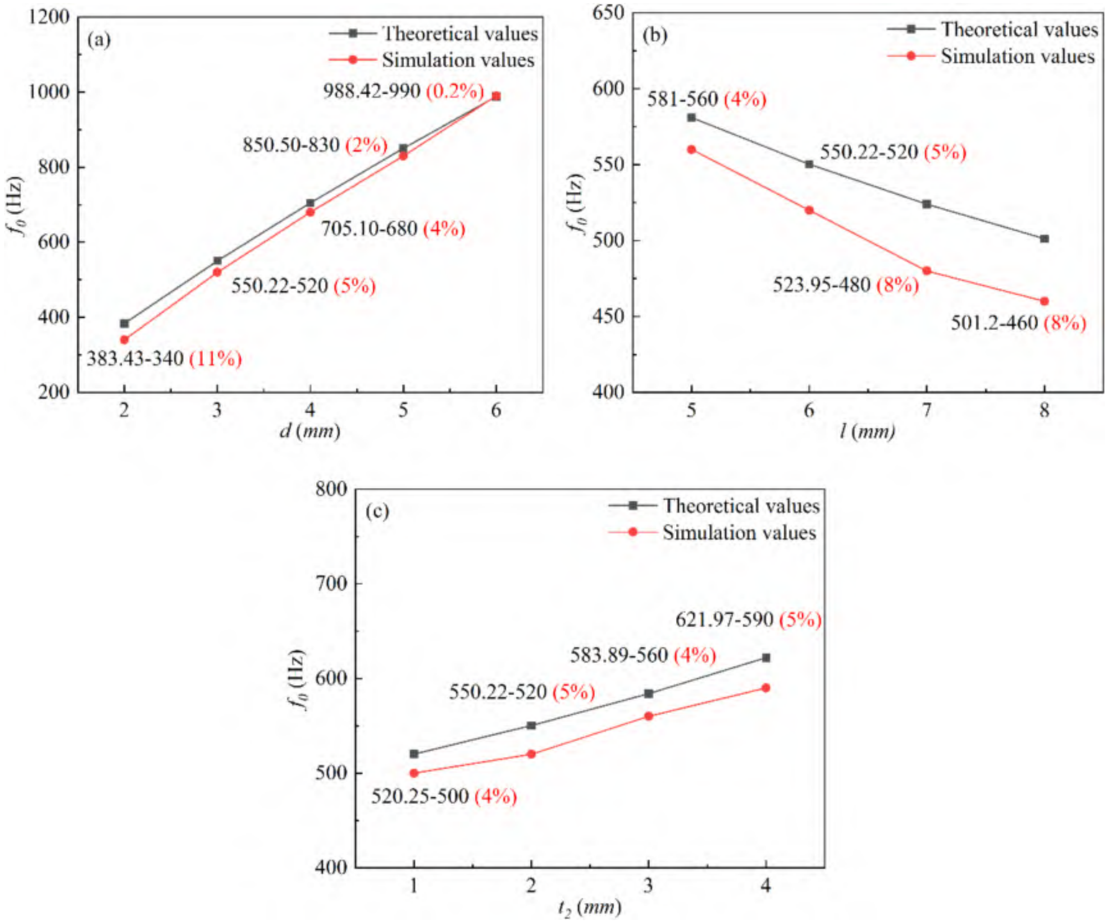

Fig. 3.7. Effects of the embedded tube diameter, embedded tube length and external structure wall thickness on the resonance frequency (a) Relationship between the diameter of the embedded tube and the resonance frequency (b) Relationship between the length of the embedded tube and the resonance frequency (c) Relationship between the external structure wall thickness and resonance frequency.

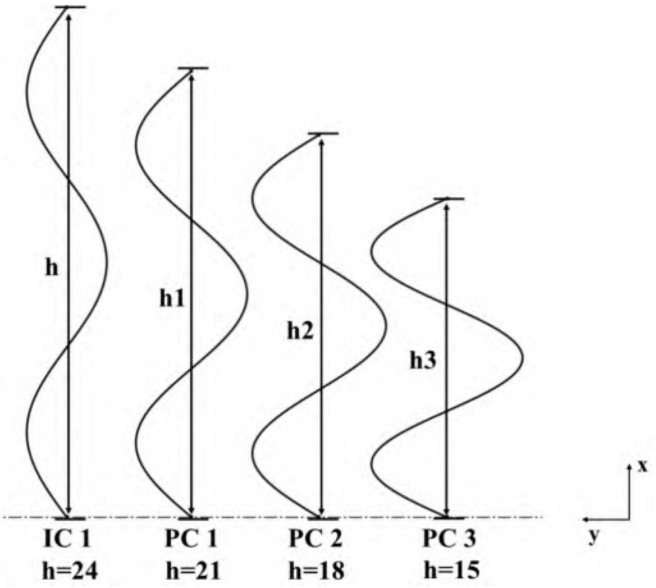

Fig. 4.1. Diagram of the arc length of each cavity wall configuration.

performance.

To confirm the reliability of this analysis, the simulation results are compared with the theoretical results shown in Fig. 3.7. Fig. 3.7(a) shows that when the diameter of the embedded tube is just 2 mm, there is a certain degree of error between the theoretical and finite element analysis results. This kind of error is caused primarily by the small size of the aperture of the resonator; thus, the wavelength of the sound wave is too large relative to the aperture, and it is difficult for it to effectively enter the resonator, which hinders the normal propagation of the sound wave and the occurrence of resonance phenomena, thus affecting the pressure and flow velocity distributions in the cavity. Therefore, the assumption that sound waves can completely enter the cavity and form a stable resonance in the theoretical calculation is different from the actual situation, resulting in an error between the theoretical calculation and the simulation results. In addition, the mismatch between the aperture and the wavelength especially affects the performance of the resonator when the aperture is very small.

When the tube length of the embedded tube in Fig. 3.7(b) is increased to 6 and 7 mm, the error increases to 8 %. This error may be due to the insufficient consideration of the actual structural boundary conditions in constructing the theoretical model and the neglect of material loss, nonideal characteristics of the tube wall and other factors. Relatively speaking, the simulation analysis is closer to the actual conditions, and these factors are simulated more comprehensively, thus explaining the difference between the theoretical values and the simulation results.

As shown in Fig. 3.7(c), the error between the simulation and theory of resonance frequency can be disregarded when the thickness of the external structure is modified. The variation trend in Fig. 3.7 shows that a reduction in the resonance frequency requires a decrease in d and t_2, and the difference is that l needs to increase. Therefore, the resonance frequency and transmission loss of the embedded tube Helmholtz resonator can be adjusted by modifying the structural parameters.

4. Reconfigurable embedded tube Helmholtz resonators based on SMP active deformation characteristics

The shape memory polylactic acid (PLA) temporary configuration can be shaped by applying external forces when the temperature exceeds the glass transition temperature. Once the temperature falls below the glass transition temperature, the model temporary configuration is fixed. In addition, reheating beyond the glass transition temperature allows the temporary configuration to return to its original shape. Relying on this characteristic, this section takes the embedded tube Helmholtz resonator as the basis, and inspired by the design concept that the SMP shape can be controlled by external field stimulation, the strategy to achieve the optimal sound insulation performance in different frequency bands by adjusting the cavity wall configuration of

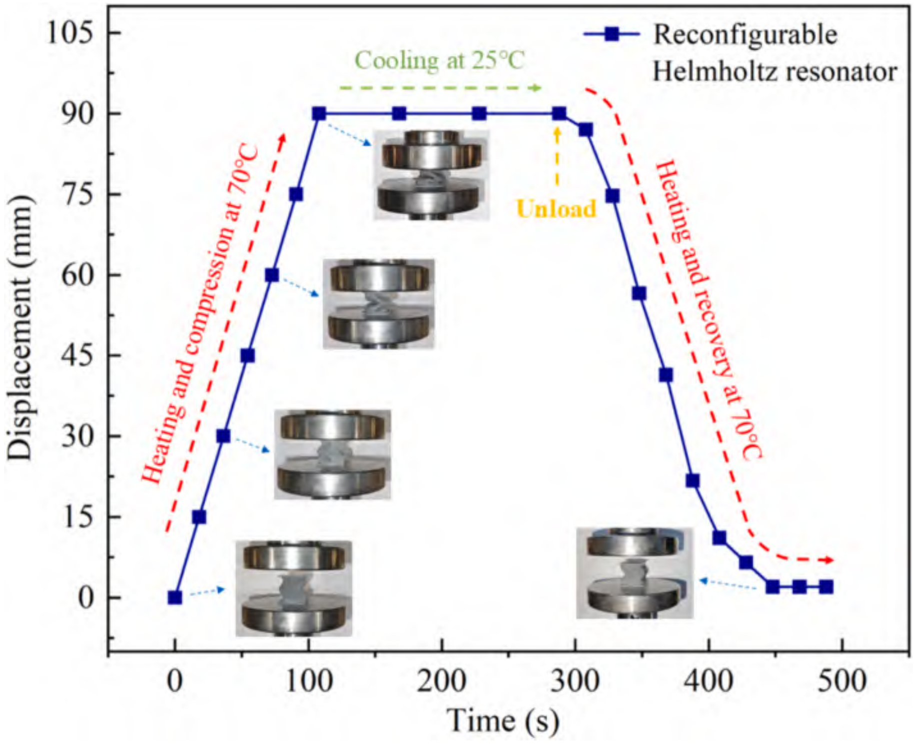

Fig. 4.2. 4D print-embedded tube Helmholtz resonator shape memory cycle experiment.

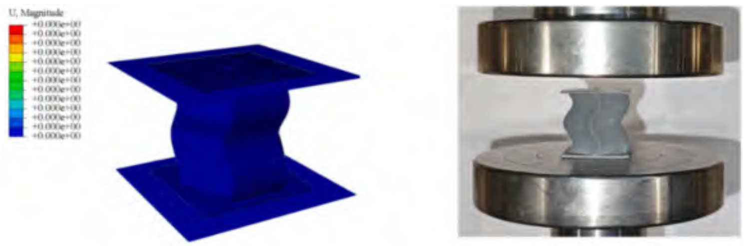

Initial configuration
(h=24mm)

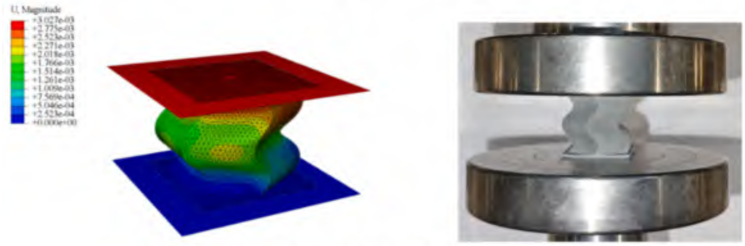

Temporary configuration I
(h=21mm)

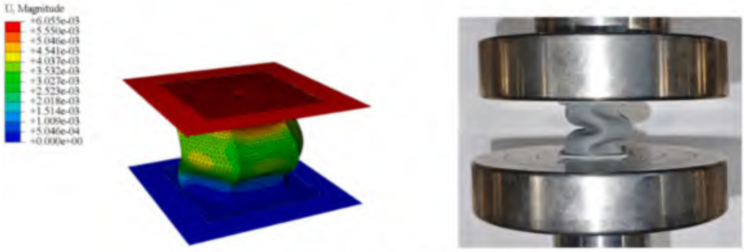

Temporary configuration II
(h=18mm)

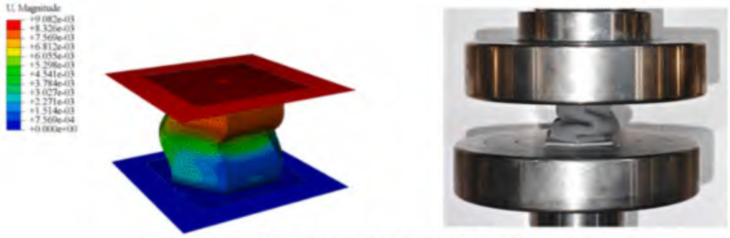

Temporary configuration III
(h=15mm)

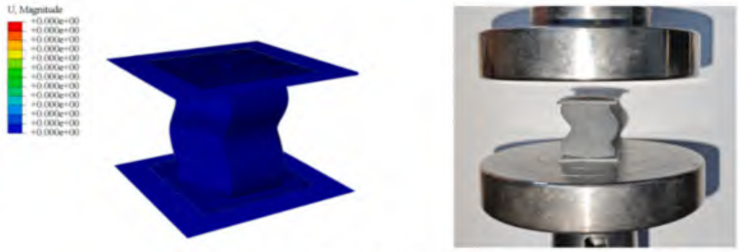

Configurational recovery
(h=24mm)

Fig. 4.3. Comparison between the simulated deformation and experimental deformation of the Helmholtz resonator under heating compression (a) Schematic diagram of the compression process after heating (b) Schematic diagram of the shape recovery process after heating.

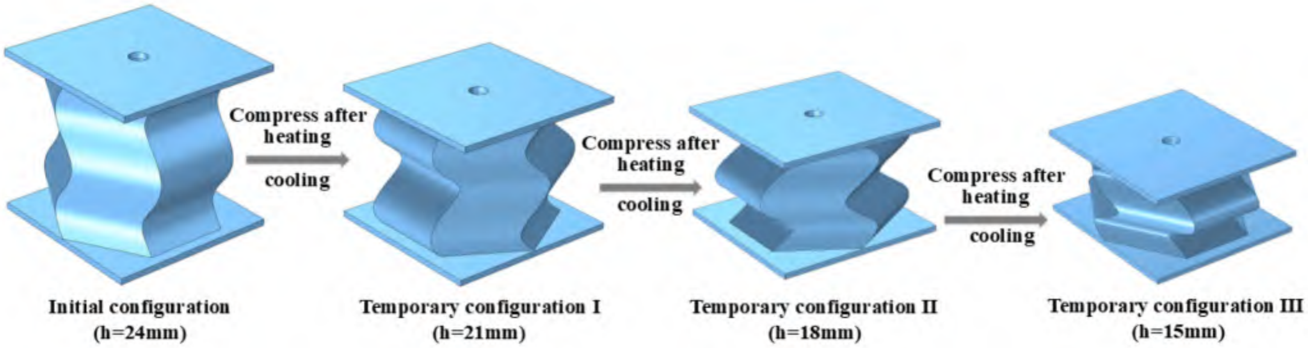

(a) Schematic diagram of the compression process after heating

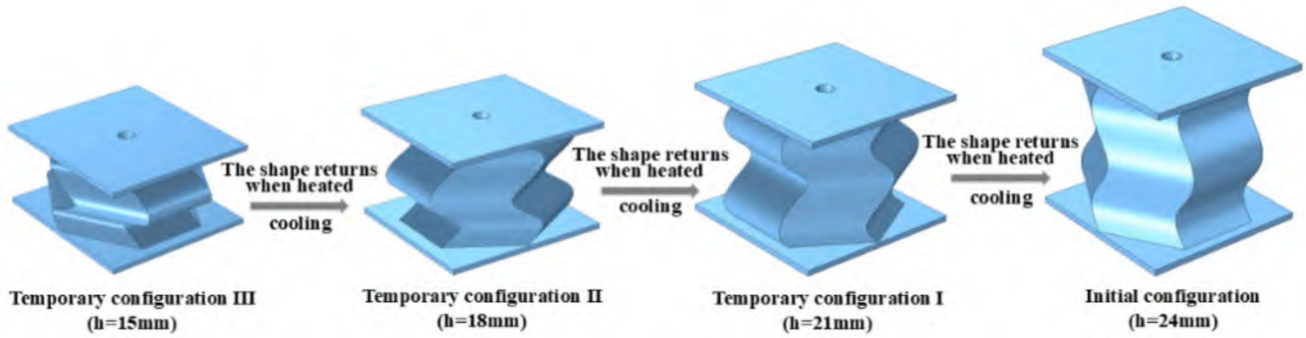

(b) Schematic diagram of the shape recovery process after heating

Fig. 4.4. Schematic diagram of cavity wall reconfiguration of embedded tube Helmholtz resonators.

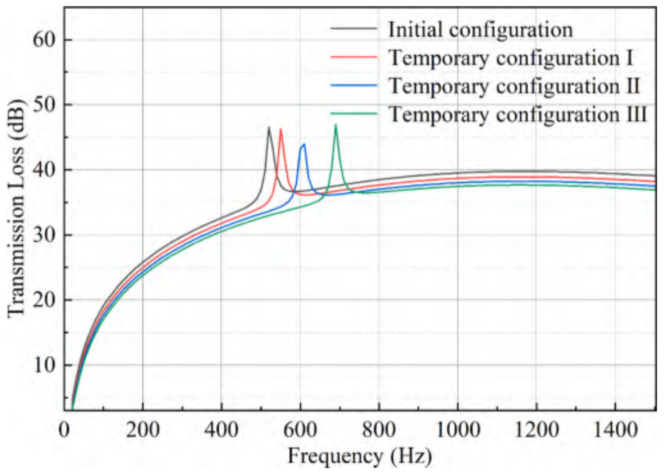

Fig. 4.5. Simulation results of the transmission loss of the reconfigurable embedded tube Helmholtz resonator.

the resonator is deeply discussed. According to the requirements of sound insulation in different frequency bands in actual application scenarios, the cavity wall configuration of the resonator can be actively adjusted to form a sound insulation peak in the corresponding frequency band to achieve the adjustable effect of macroacoustic performance. This research not only enhances the adaptability and flexibility of resonators but also offers a theoretical foundation and practical guidance for achieving the acoustic performance requirements in various application scenarios.

$$y = A\sin\left(\frac{3\pi}{h}x\right) \tag{10}$$

$$s = \sqrt{(dx)^2 + (dy)^2} = \int \sqrt{1 + (y')^2}dx \tag{11}$$

Among them, the cavity wall configuration is formed by sinusoidal boundary–surface rotation. According to the sine formula and arc length formula and to ensure the consistency of the arc length of each cavity wall configuration, the cavity height h is adjusted by using the active deformation characteristic of the reconfigurable embedded tube Helmholtz resonator (as shown in Fig. 4.1).

The shape memory polylactic acid Helmholtz resonator made by 4D printing technology can sense changes in the external environment and actively respond to it, realizing the shape memory cycle of “initial state-temporary morphing-return to the initial state.” As shown in Fig. 4.2, the resonator is heated at 70 °C ($>Tg$, rubber state) and compressed to different temporary configurations at a loading rate of 5 mm/min (as shown in Fig. 4.3). During the cooling phase, the temperature is uniformly reduced from 70 °C to room temperature (approximately 25 °C $<Tg$, glassy state), during which the temporary configuration is always maintained.

At the end of the cooling phase, the mechanical load on the resonator is removed, and the resonator remains in its temporary configuration, indicating that the resonator has an almost perfect shape fixation rate. The resonator is in the shape recovery phase from 288 s to 488 s. When the temperature increases from room temperature to 70 °C, owing to the SMP shape memory effect, the temporary configuration of the resonator starts to return to the initial configuration, and the shape recovery rate is as high as 99.23 %.

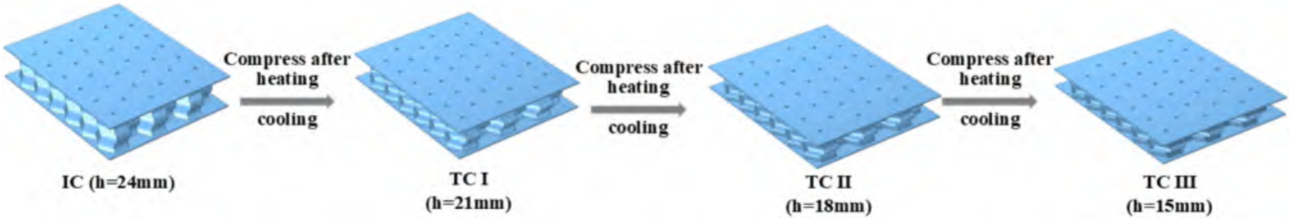

Fig. 5.1. Schematic diagram of the reconfiguration of a metamaterial honeycomb sandwich panel.

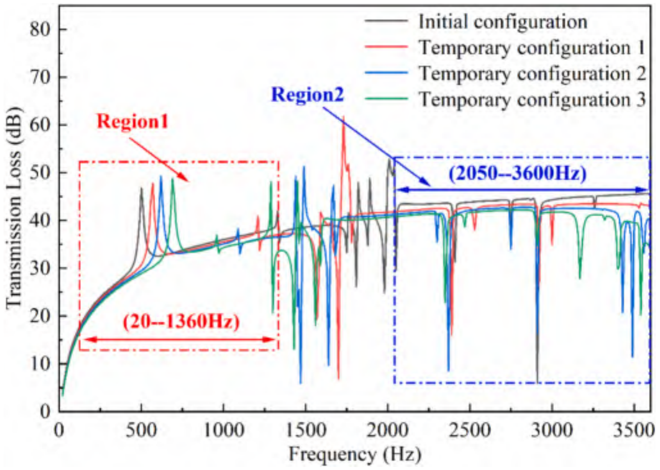

Fig. 5.2. Simulation results of the transmission loss of a reconfigurable metamaterial honeycomb sandwich panel.

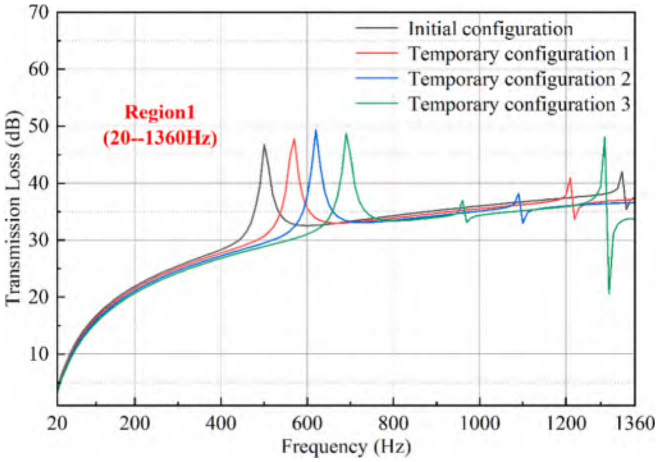

Fig. 5.3. Simulation results of transmission loss of reconfigurable metamaterial honeycomb sandwich panels in Region 1 (20–1360 Hz).

The reconfigurable embedded tube Helmholtz resonator allosteric process is shown in Fig. 4.4. First, the resonator is heated above the glass transition temperature. Axial compression causes the resonator to buckle, and the cavity height *h* is compressed from the initial 24 mm to 21 mm. When cooled, the structure can maintain the temporary configuration I shown in Fig. 4.4(a), at which point the resonator exhibits the corresponding temporary acoustic properties. When the desired acoustic characteristics are adjusted according to changes in the operating environment, the resonator is reheated above the glass transition temperature, and the cavity height is reduced from 21 mm to 18 mm by further axial compression. After cooling, the resonator can maintain the temporary configuration II shown in Fig. 4.4(a) and has the acoustic characteristics of the configuration. According to this working principle, the temporary configuration III shown in Fig. 4.4(a) and its specific temporary acoustic characteristics can also be realized, and the acoustic performance of each configuration of the resonator is shown in Fig. 4.5.

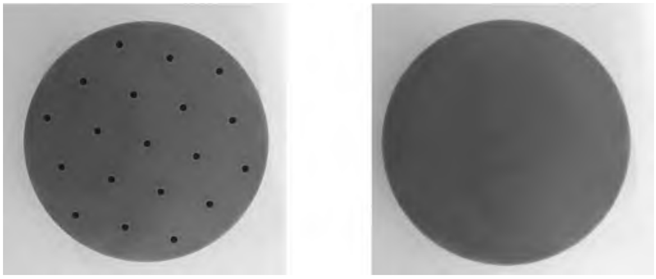

Fig. 6.1. Acoustic sample of a reconfigurable metamaterial honeycomb sandwich panel.

In addition, when the working environment changes and the acoustic characteristics of the initial configuration of the resonator are again needed, the structure can be heated above the glass transition temperature, and the acoustic characteristics can be restored to the initial acoustic characteristics. The smooth and continuous adjustment of the acoustic characteristics of reconfigurable embedded tube Helmholtz resonators can be achieved by controlling the on-heating time.

5. Reconfigurable metamaterial honeycomb sandwich panels based on the active deformation characteristics of SMPs

In this section, a finite element model of reconfigurable metamaterial honeycomb sandwich panels consisting of 36 embedded tube Helmholtz resonators is established. Fig. 5.1 shows the initial configuration and three temporary configurations of the reconfigurable metamaterial honeycomb sandwich panel.

In this section, the acoustic insulation characteristics of the initial configuration and three temporary configurations of the reconfigurable metamaterial honeycomb sandwich panel are analyzed in detail. As illustrated in Fig. 5.2, acoustic simulation software was employed to obtain transmission loss simulation results for the reconfigurable metamaterial honeycomb sandwich pane.

Fig. 5.2 displays the simulation results indicating that within frequency region 1 (20–1,360 Hz), the sound insulation performance of metamaterial honeycomb sandwich panels can be intelligently and actively regulated according to the sound insulation peak frequency bands of four kinds of configurations. In frequency region 2 (2,050–3,600 Hz), owing to the exceptional sound insulation performance exhibited by the initial configuration in this region, the temporary configuration is restored to the initial configuration by heating so that its acoustic performance is restored to the initial acoustic characteristics. This strategy provides the optimal control combination of sound insulation characteristics. In addition, Fig. 5.3 is a local enlargement of region 1 (20–1,360 Hz) in Fig. 5.2, which more clearly shows the characteristics of the four configurations of sound insulation peak

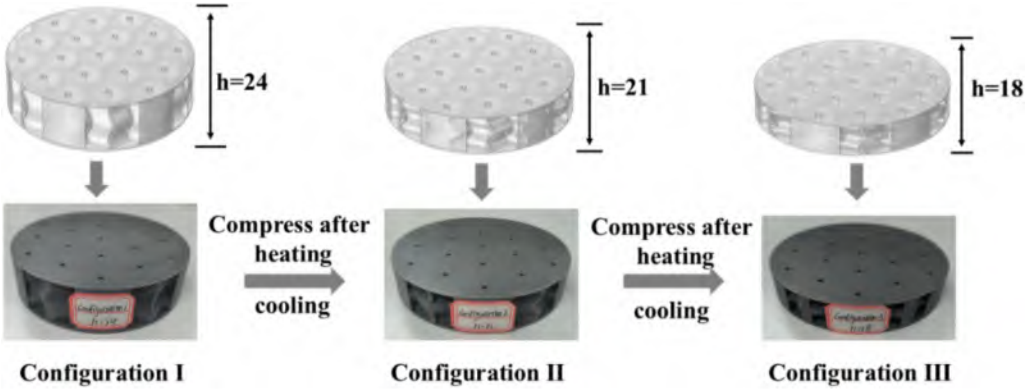

Fig. 6.2. Allosteric process of the acoustic sample.

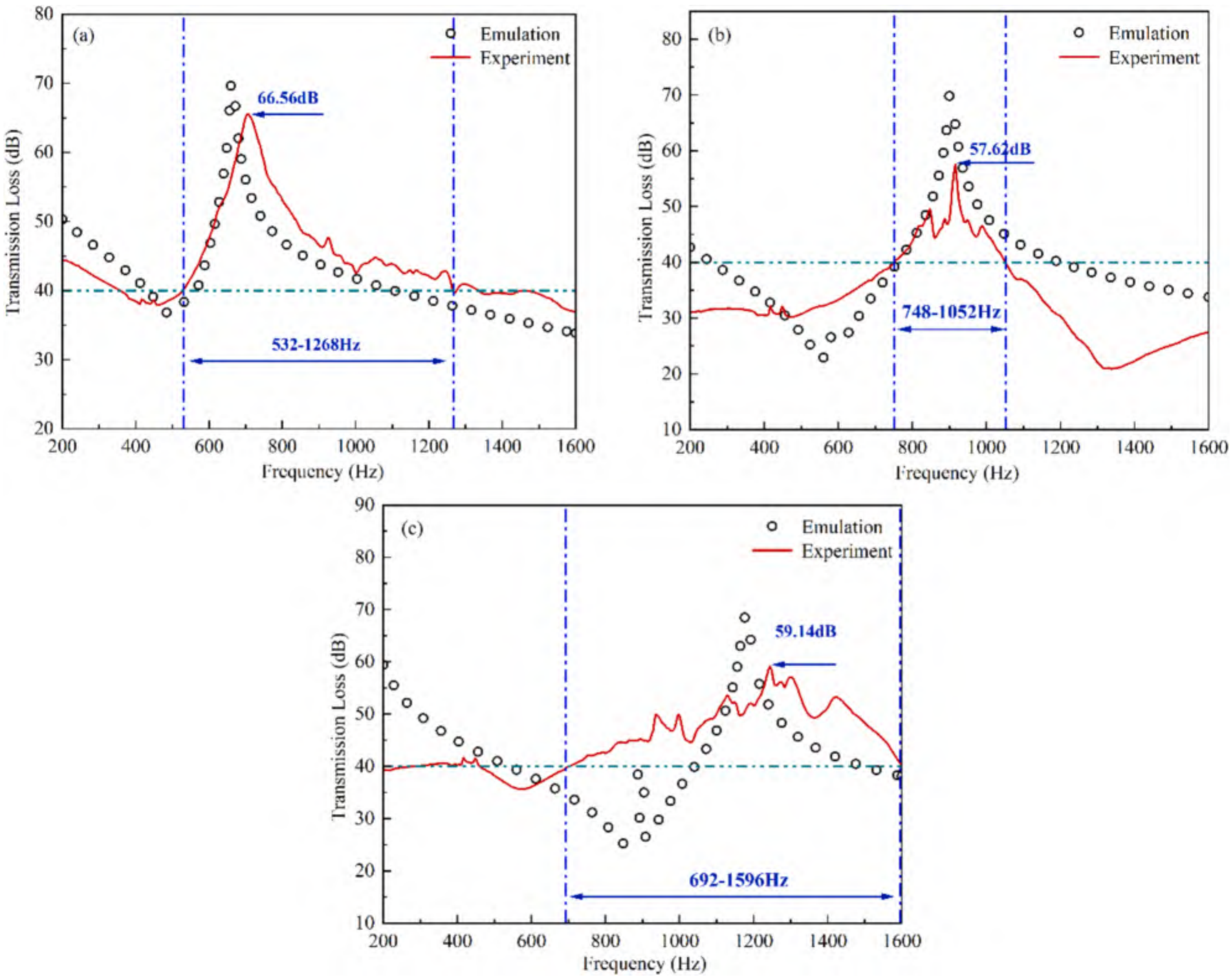

Fig. 6.3. Results of transmission loss in each configuration of the acoustic sample (a) Transmission loss experiment and simulation diagram of configuration I (b) Transmission loss experiment and simulation diagram of configuration II (c) Transmission loss experiment and simulation diagram of configuration III.

frequency bands that can be intelligently and actively regulated in this frequency band.

The reconfigurable metamaterial honeycomb sandwich panels effectively utilize the active deformation characteristics of SMPs. Through this SMP characteristic, the microstructure of the reconfigurable metamaterial honeycomb sandwich panel can be reconstructed, and the macroacoustic performance can be flexibly adjusted. This design strategy, which is based on microstructure reconfiguration and macroacoustic performance adjustment, not only significantly enhances the flexibility and adaptability of sound insulation performance but also shows the great potential of metamaterial honeycomb sandwich panels in the intelligent active control of acoustic performance field.

Table 6.1
Numerical statistics of the TL curves of reconfigurable honeycomb sandwich panels.

Configuration/mm	The highest STL/ dB	Optimal frequency range of STL/ Hz
Configuration I/(h = 24)	66.56	532–1268
Configuration II/(h = 21)	57.62	748–1052
Configuration III/(h = 18)	59.14	692–1600

6. Experimental study of the sound insulation of reconfigurable metamaterial honeycomb sandwich panels

Fig. 6.1 displays the acoustic sample of the reconfigurable metamaterial honeycomb sandwich panel prepared via 4D printing technology. The reconfigurable metamaterial honeycomb sandwich panel has a complex geometry. Therefore, an SMP polylactic acid filament with an almost perfect shape memory effect was used as a printing material to prepare it by melt deposition 4D printing integrated molding technology. In addition, Fig. 6.2 displays allosteric process of the acoustic sample.

To measure the transmission loss, a Bruel & Kjaer dual-microphone impedance tube (Model 4206) is used and measured in accordance with the standard procedure detailed in ASTM (E2611-17). The measured frequency range is 200–1600 Hz, and the sample diameter is 99.5 mm.

Considering the constraint problem of the sample in the impedance tube experiment, the real constraint conditions around the sample in the experiment were simulated by finite element simulation, that is, fixed constraints consistent with the experiment were introduced in the simulation to ensure the consistency of the experiment and simulation. Fig. 6.3 shows the transmission loss results of each configuration of the reconfigurable metamaterial honeycomb sandwich panel obtained through simulation and experimental measurements. The results show that the experimental results closely align with the finite element simulation results. However, it should be noted that the experimental results are slightly lower than the simulation results in the peak frequency range because the ideal environmental factors in the simulation cannot be fully simulated during the experiment, such as background sound pressure field and boundary conditions.

Table 6.1 shows the numerical statistics of the TL curve in Fig. 6.3. The analysis results indicate that configuration I achieves a peak sound insulation value of 66.56 dB within the frequency range of 532–1268 Hz, which is significantly better than those of the other two configurations, and the sound insulation band is wide. Configuration II has the narrowest sound insulation band and the lowest sound insulation peak. Configuration III features the widest sound insulation peak frequency band along with a high sound insulation peak value.

The reconfigurable metamaterial honeycomb sandwich panel not only offers a wider sound insulation peak frequency band and a higher sound insulation peak but can also meet different sound insulation requirements by changing its configuration. These results verify the theory proposed in this paper; that is, by actively adjusting the cavity wall configuration of the resonator, the sound insulation peak can be formed in the desired frequency band based on the sound insulation requirements of different frequency bands in practical applications, achieving adjustable macroacoustic performance.

7. Analysis of sound insulation performance of reconfigurable metamaterial honeycomb sandwich panels with different configurations

As shown in Fig. 7.1, the wave number of the reconfigurable metamaterial honeycomb sandwich panel was changed to study its sound insulation performance while maintaining the same configuration arc length. It can be observed from Fig. 7.2 that the change of wave number

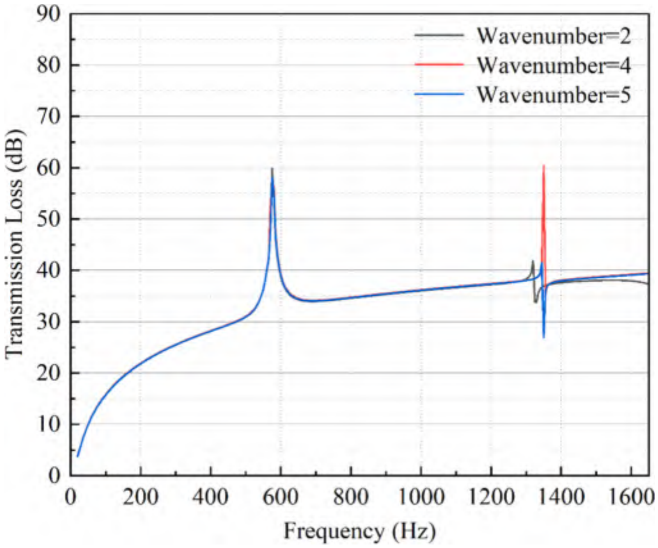

Fig. 7.2. Sound insulation performance analysis of reconfigurable metamaterial honeycomb sandwich panels with different wave numbers.

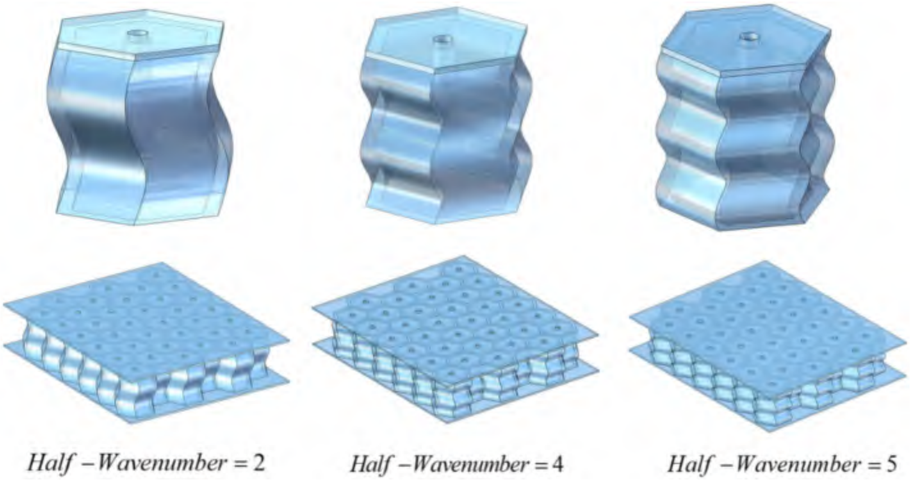

Fig. 7.1. Reconfigurable metamaterial honeycomb sandwich panels with different wave numbers and the same arc length.

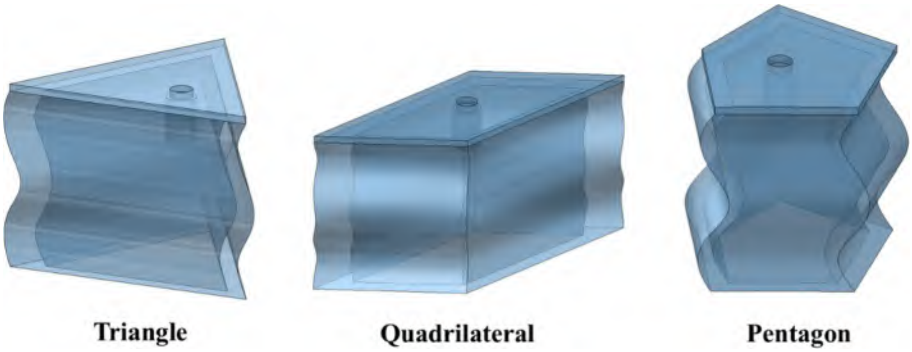

Fig. 7.3. Triangular, quadrilateral, and pentagonal unicellular cells.

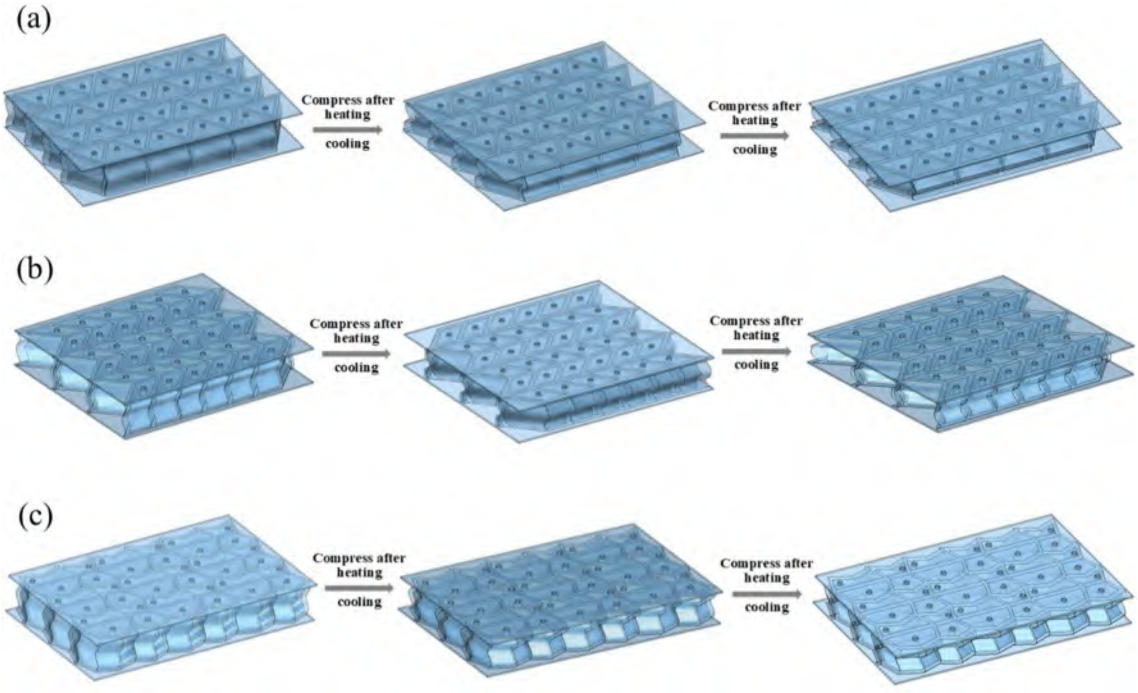

Fig. 7.4. Reconfigurable metamaterial honeycomb sandwich panels with different configurations.

Table 7.1
Performance comparison of reconfigurable metamaterial honeycomb sandwich panels with different configurations within 1600 Hz frequency range.

configuration	sound insulation effect	stability
triangular	inferior	moderate
quadrilateral	optimal	inferior
pentagonal	moderate	optimal

has little effect on the sound insulation performance of the honeycomb sandwich panel. This is because, on the premise of keeping the arc length of the configuration unchanged, the change of the wave number of the sine function will only lead to a slight change in the configuration of the cavity wall of the structure, and the propagation path of the sound wave is almost unchanged, so the sound insulation performance tends to be consistent.

Based on the above research on hexagonal reconfigurable metamaterial honeycomb sandwich panels, this section discusses the sound insulation performance of honeycomb sandwich panels with different configurations under the same volume conditions. Fig. 7.3 and Fig. 7.4 show the single cell structures of different configurations and the honeycomb sandwich panels composed of them, respectively. Table 7.1 compares the sound insulation performance and stability of reconfigurable metamaterial honeycomb sandwich panels with different configurations. First, it can be observed from Fig. 7.5(a) and Table 7.1 that triangular honeycomb sandwich panels exhibit two significant peaks in sound insulation performance. However, in the middle and high frequency bands, the sound insulation effect of the structure fluctuates greatly. This is due to the simplicity of the triangular structure, so that small geometric changes can significantly change the reflection path, thereby increasing the energy dissipation and improving the sound insulation effect.

Next, it can be seen from the analysis of Fig. 7.5(b) that quadrilateral honeycomb sandwich panel has the best performance in sound insulation effect, but it also shows greater fluctuation. This phenomenon is mainly because the quadrilateral structure contains sharper angles, resulting in the reflection path concentrated in these areas, thus increasing the number of reflections and energy dissipation.

Finally, Fig. 7.5(c) shows that the pentagonal honeycomb sandwich panel has excellent sound insulation performance and stability, and has continuous sound insulation peaks. This excellent performance is attributed to the fact that the honeycomb sandwich panel shown in Fig. 7.4(c) consists of four pentagons of different configurations, the

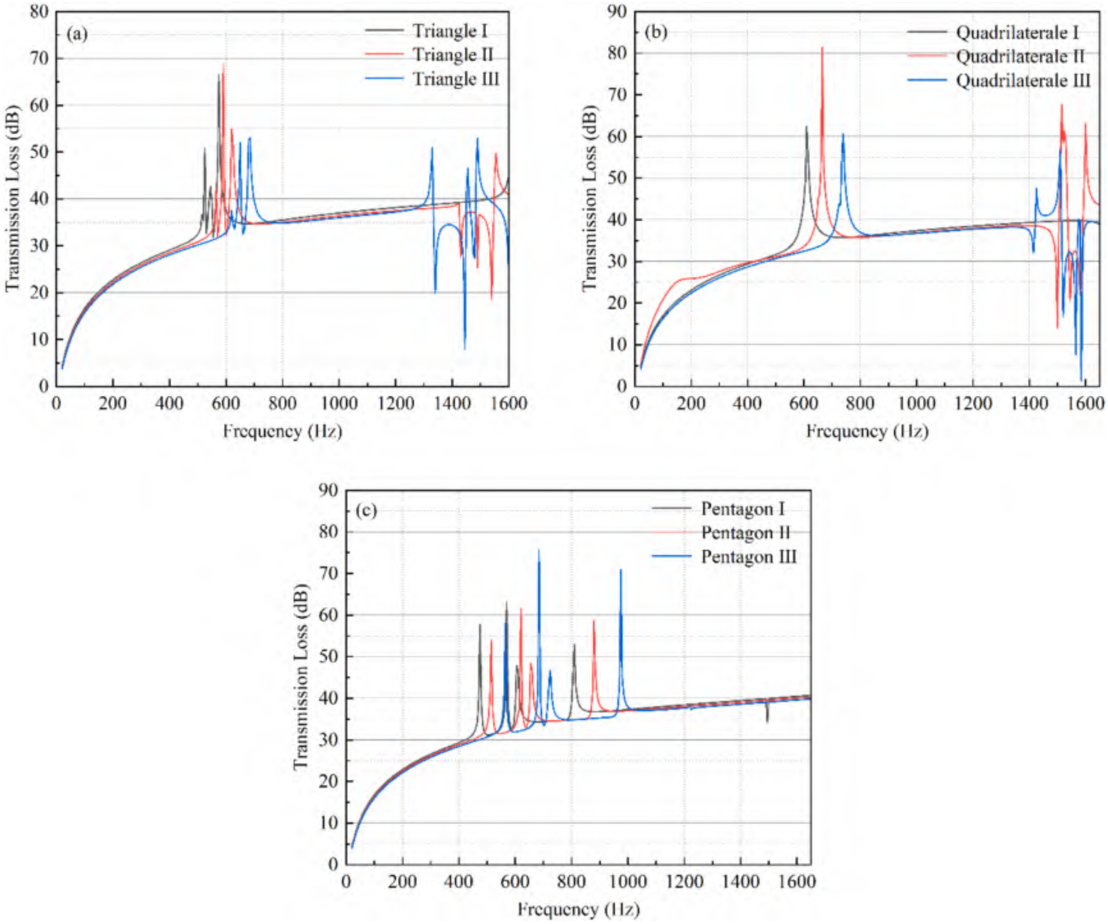

Fig. 7.5. Sound insulation performance analysis of reconfigurable metamaterial honeycomb sandwich panels with different configurations (a) Sound insulation performance of triangular honeycomb sandwich panel (b)Sound insulation performance of quadrangle honeycomb sandwich panel **(c)** Sound insulation performance of pentagonal honeycomb sandwich panel.

combination of which effectively enhances the number and effect of sound insulation peaks. These findings provide an important basis for subsequent research.

8. Conclusion

In this paper, a reconfigurable metamaterial honeycomb sandwich panel based on microstructure reconfiguration and macroacoustic performance adjustment is developed by taking advantage of the active deformation characteristics of SMPs. This approach is highly important for noise reduction and the acoustic stealth design of equipment operating in complex mechanical environments. The conclusions are as follows.

With the decrease in the diameter of the embedded tube and the thickness of the external structure, the resonance frequency of the embedded tube Helmholtz resonator exhibits a corresponding reduction. In contrast, a shortening of the tube length leads to an increase in its resonance frequency. Moreover, the influence of structural parameter variation on the resonance frequency (transmission loss) of the embedded tube Helmholtz resonator is systematically verified by theoretical and simulation results.

The shape memory effect of the Helmholtz resonators was verified via the 4D printing of SMP material. By modifying the cavity wall configuration of the resonator, the optimal sound insulation performance was achieved across different frequency bands.

In the middle- and high-frequency bands, the initial configuration of the reconfigurable metamaterial honeycomb sandwich panel demonstrates exceptional sound insulation performance. In the low-frequency range, the sound insulation performance of the reconfigurable metamaterial honeycomb sandwich panel can be intelligently adjusted under four configurations.

Drawing upon the outcomes of finite element simulations and experimental investigations, we concluded that the reconfigurable metamaterial honeycomb sandwich panel not only exhibits a wider peak frequency band for sound insulation and a higher sound insulation peak but can also meet different sound insulation requirements by changing its configuration.

When the structural arc length of the reconfigurable metamaterial honeycomb sandwich panel remains unchanged, the change of wave number has little effect on its sound insulation performance. In addition, under the same volume conditions, the triangular honeycomb sandwich panel has week sound insulation performance, but its stability is well. The quadrangle honeycomb sandwich panel has the best sound insulation performance, but the stability is the worst. Pentagonal honeycomb sandwich panel has good sound insulation performance and stability.

CRediT authorship contribution statement

Hui Wang: Writing – review & editing, Writing – original draft, Visualization, Formal analysis, Conceptualization. **Yaxiang Sun:** Writing – review & editing, Project administration, Investigation. **Xin Lan:** Writing – review & editing, Visualization, Project administration. **Hanxing Zhao:** Writing – review & editing, Supervision, Data curation. **Yong-Hua Yu:** Writing – review & editing, Investigation. **Weichun Huang:** Writing – review & editing, Project administration. **Yanju Liu:**

Writing – review & editing, Supervision, Project administration. **Jingsong Leng:** Writing – review & editing, Project administration, Conceptualization.

Declaration of competing interest

The authors declare that they have no known competing financial interests or personal relationships that could have appeared to influence the work reported in this paper.

Acknowledgements

This work is supported by the National Key R&D Program of China (2022YFB3805700), the Postdoctoral Fellowship Program of CPSF under Grant Number GZB20240963, the Heilongjiang postdoctoral fund under Grant Number LBH-Z23192, the National Natural Science Foundation of China (Grant No. 12272113).

Data availability

Data will be made available on request.

References

[1] Chen CM, Guo ZF, Liu ST, Feng HD, Qiao CX. Hybrid acousto-elastic metamaterials for simultaneous control of low-frequency sound and vibration. J Appl Phys 2021;129.

[2] Song H, Ding XD, Cui ZX, Hu HH. Research progress and development trends of acoustic metamaterials. Molecules 2021;26.

[3] Liu ZY, Zhang XX, Mao YW, Zhu YY, Yang ZY, Chan CT, et al. Locally resonant sonic materials. Science 2000;289:1734–6.

[4] Sigalas MM, Economou EN. Acoustic band-structure of periodic elastic composites - comment. Phys Rev Lett 1995;75:3580.

[5] Gao NS, Zhang ZC, Deng J, Guo XY, Cheng BZ, Hou H. Acoustic metamaterials for noise reduction: a review. Adv Mater Technol 2022;7.

[6] Mei J, Ma GC, Yang M, Yang ZY, Wen WJ, Sheng P. Dark acoustic metamaterials as super absorbers for low-frequency sound. Nat Commun 2012;3.

[7] Gu YH, Zhong HB, Bao B, Wang Q, Wu JH. Experimental investigation of underwater locally multi-resonant metamaterials under high hydrostatic pressure for low frequency sound absorption. Appl Acoust 2021;172.

[8] Zhong HB, Gu YH, Bao B, Wang Q, Wu JH. 2D underwater acoustic metamaterials incorporating a combination of particle-filled polyurethane and spiral-based local resonance mechanisms. Compos Struct 2019;220:1–10.

[9] Fang N, Xi DJ, Xu JY, Ambati M, Srituravanich W, Sun C, et al. Ultrasonic metamaterials with negative modulus. Nat Mater 2006;5:452–6.

[10] Shen YC, Yang YY, Guo XS, Shen Y, Zhang D. Low-frequency anechoic metasurface based on coiled channel of gradient cross-section. Appl Phys Lett 2019;114.

[11] Jang JY, Song KYJ. Synergistic acoustic metamaterial for soundproofing: combining membrane and locally resonant structure. Int J Mech Sci 2023;256.

[12] Du Y, Wu WG, Chen W, Lin YS, Chi QJ. Control the structure to optimize the performance of sound absorption of acoustic metamaterial: a review. Aip Adv 2021;11.

[13] Ma GC, Sheng P. Acoustic metamaterials: from local resonances to broad horizons. Sci Adv 2016;2.

[14] Liu ZB, Rumpler R, Feng LP. Locally resonant metamaterial curved double wall to improve sound insulation at the ring frequency and mass-spring-mass resonance. Mech Syst Sig Process 2021;149.

[15] Xin YJ, Huang RN, Li P, Qian Q, Yan Q, Sun YT, et al. Labyrinthine acoustic metamaterials with triangular self-similarity for low-frequency sound insulation at deep subwavelength dimensions. Res Phys 2023;54.

[16] Langfeldt F, Khatokar AJ, Gleine W. Plate-type acoustic metamaterials with integrated Helmholtz resonators. Appl Acoust 2022;199:109019.

[17] Gai XL, Guan XW, Cai ZN, Li XH, Hu WC, Xing T, et al. Acoustic properties of honeycomb like sandwich acoustic metamaterials. Appl Acoust 2022;199.

[18] Yamamoto T. Acoustic metamaterial plate embedded with Helmholtz resonators for extraordinary sound transmission loss. J Appl Phys 2018;123.

[19] Yuan M, Yang F, Pang Z. Deep subwavelength split ring neck acoustic resonator. Results Phys 2019;13:102322.

[20] Sharafkhani N. A helmholtz resonator-based acoustic metamaterial for power transformer noise control. Acoust Aust 2022;50:71–7.

[21] Wei S, Li L, Zhigang C, Linyong L, Xiaopeng F. A parameter design method for multifrequency perfect sound-absorbing metasurface with critical coupled Helmholtz resonator. J Low Frequency Noise, Vibration and Active Control 2021;40:2054–63.

[22] Hu PZ, Zhao JB, Liu H, Zhang XS, Yao H, Zhang GJ. Low-frequency acoustic isolation performance of Helmholtz cavity acoustic metamaterials with bilateral single openings. Aip Adv 2024;14.

[23] Huang S, Fang XS, Wang X, Assouar B, Cheng Q, Li Y. Acoustic perfect absorbers via Helmholtz resonators with embedded apertures. J Acoust Soc Am 2019;145:254–62.

[24] Hu PZ, Zhao JB, Liu H, Zhang XS, Zhang GJ, Yao H. Low-frequency sound-insulation performance of labyrinth-type helmholtz and thin-film compound acoustic metamaterial. Materials 2024;17.

[25] Huang YL, Gao N, Chen WQ, Bao RH. Extension/compression-controlled complete band gaps in 2D chiral square-lattice-like structures. Acta Mech Solida Sin 2018;31:51–65.

[26] Zhao HX, Mu T, Lan X, Liu LW, Liu YJ, Leng JS. Microbuckling behavior of unidirectional fiber-reinforced shape memory polymer composite undergoing compressive deformation. Compos Struct 2022;297.

[27] Zhao W, Li N, Liu LW, Leng JS, Liu YJ. Mechanical behaviors and applications of shape memory polymer and its composites. Appl Phys Rev 2023;10.

[28] Zhang JF, Yin ZF, Ren LQ, Liu QP, Ren L, Yang X, et al. Advances in 4D printed shape memory polymers: from 3D printing, smart excitation, and response to applications. Adv Mater Technol 2022;7.

[29] Zhao W, Liu LW, Lan X, Su B, Leng JS, Liu YJ. Adaptive repair device concept with shape memory polymer. Smart Mater Struct 2017;26.

[30] Ohki T, Ni QQ, Iwamoto M. Creep and cyclic mechanical properties of composites based on shape memory polymer. Sci Eng Compos Mater 2004;11:137–47.

[31] Liu YJ, Du HY, Liu LW, Leng JS. Shape memory polymers and their composites in aerospace applications: a review. Smart Mater Struct 2014;23.

[32] Xia YL, He Y, Zhang FH, Liu YJ, Leng JS. A review of shape memory polymers and composites: mechanisms, materials, and applications. Adv Mater 2021;33.

[33] Liu TZ, Zhao W, Yao YT, Lin C, Zhao HX, Cai JG. Mechanical and shape-memory properties of TPMS with hybrid configurations and materials. Int J Smart Nano Mater 2024.

[34] Zhao F, Zheng XY, Zhou SC, Zhou B, Xue SF, Zhang Y. Constitutive model for epoxy shape memory polymer with regulable phase transition temperature. Int J Smart Nano Mater 2021;12:72–87.

[35] Xu PL, Lan X, Zeng CJ, Leng JS, Liu YJ. Active vibration control effect of 3D printed cruciform honeycomb laminates based on fiber-reinforced shape memory polymer. Compos Struct 2024;346.

[36] Wang X, He Y, Xiao X, Zhao W, Leng J. High-Tg shape memory polyimide composites with “spot-plane” directional thermally conduction structure based on AlN nanoparticles and acidified graphene. Compos Struct 2024;330:117846.

[37] Alshahrani HA. Review of 4D printing materials and reinforced composites: Behaviors, applications and challenges. J Sci-Adv Mater Devices 2021;6:167–85.

[38] Rafiee M, Farahani RD, Therriault D. Multi-material 3D and 4D printing: a survey. Adv Sci 2020;7.

[39] Fu P, Li HM, Gong J, Fan ZJ, Smith AT, Shen KY, et al. 4D printing of polymers: techniques, materials, and prospects. Prog Polym Sci 2022;126.

[40] Amplitude and Frequency Regulation Mechanism and Design Application via Helmholtz Resonator with Embedded Pipes. Noise and Vibration Control. 2023;43:62-8.